Emission characteristics of water in the Universe

Poelman, Dieter Roel

Chapter 6

Detecting the snow-line: water emission from proto-planetary disks

Besides being a reservoir of accreting material onto a newly formed star, the study of circumstellar disks not only sheds light on the formation mechanisms of stars, but also on the formation of planets, formed within these disks. Models that calculate the thermal and chemical structure throughout the disk are combined with radiative transfer tools in order to investigate the water emissivity in a disk around a typical T Tauri star. We find that rotational transitions are observable for sufficient integration times with upcoming instruments such as HIFI on the *Herschel Space Observatory* and EXES on SOFIA. Fluorescent ro-vibrational transitions around 6 μm tend to have stronger fluxes, observable with the aforementioned instruments. Their emissivity characteristics depend strongly on the adopted dust properties, in that lower dust opacities, i.e., up to a factor of 1000, increase the line strengths by orders of magnitude. We find that the flux of the fluorescent lines drops when freeze-out is included, and that this has an observable effect on the line profiles as well. Hence, future observations of the 6 μm fluorescent transitions will be helpful to constrain the position of the snow-line in circumstellar disks.

Based on Meijerink, R., Poelman, D. R., Spaans, M., & Tielens, A. G. G. M., in preparation

6.1 Introduction

The habitable zone within a solar system is defined as the region favourable for sustaining life as it is found on Earth. One of the conditions to provide life is that the surface of the planet maintains liquid water. However, Morbidelli et al. (2000) pointed out that the regions where such planets exist, were too hot to allow hydration of the planetesimals and protoplanets at the time of formation. They proposed a scenario in which circumstellar material was accreted from beyond 2.5 AU, where the asteroid belt contains objects that are sufficiently water-rich, i.e., where the temperature is low enough for the water to remain present in solid form on the surface. The inner edge of the region in a protoplanetary disk, where the dust temperature at the mid-plane falls below the water sublimation temperature, is generally called the snow-line. This temperature is between 145 K and 170 K depending on the water vapour pressure (Podolak & Zucker 2004). Although it is possible to evaporate grains when they are not shielded from ultraviolet (UV) photons, the opacities are too high to dissipate icy grains in the mid-plane of a disk. The photodesorption yield (molecules per photon) of water-ice is very low ($\sim 0.2\%$ for low UV fluxes), and as a consequence the H_2O desorption rate is orders of magnitudes lower than the accretion rate (Westley et al. 1995; Andersson et al. 2006). This border is of particular interest, as it has a special role in planet-formation. It is generally believed that giant planets are formed beyond this snow-line as first pointed out by Hayashi (1981). Unfortunately, the location of the snow-line in a planet-forming disk is very uncertain. Hayashi (1981) finds that the snow-line is located at about 2.7 AU for our own Solar System. This position can change in a disk around a T Tauri star, depending on the disk mass, opacity, and accretion rate. As a result, Sasselov & Lecar (2000) determined that the snow-line in this phase varies between 0.7 AU and 1.3 AU for a star with mass $M_\star = 0.5\,M_\odot$, depending on the accretion rate between 0 and $10^{-8}\,M_\odot$/yr and an assumed sublimation temperature of $T = 170$ K. Lecar et al. (2006) finds that dust opacity, disk mass and/or accretion rates have to be increased up to an order of magnitude to shift the snow-line from 1.6 – 1.9 AU past 2.7 AU (for an adopted minimum mass disk of $0.02\,M_\odot$, conventional dust opacities and an accretion rate of $10^{-8}\,M_\odot$/yr). Garaud & Lin (2007) find that the snow-line around T Tauri stars evolves from 10 AU during the FU Orionus outbursts, to 2 AU during the quasi-steady accretion phase, to 0.7 AU when the accretion rate falls below 10^{-9} $M_\odot$/yr and expands again when it goes through the protostellar-to-debris disk transition at which the disk becomes optically thin. Unfortunately, up to now the place of the snow-line has not been determined observationally in protoplanetary disks around T Tauri stars.

Water is very abundant in the gas phase at temperatures between the dissociation temperature, $T \sim 2500$ K, and the water-ice sublimation tem-

perature, $T \sim 145 - 170$ K. Carr et al. (2004) and Thi & Bik (2005) observed warm H_2O gas at temperatures $T > 1200$ K and radii $R < 0.4$ AU from observations of high-lying, ro-vibrational lines around 2.3 μm. Unfortunately, water at the temperature of interest is hard to observe from the ground. Although H_2O can sample a large range of physical conditions due to its very rich ro-vibrational and rotational spectrum in the near- and far-infrared, atmospheric H_2O has a large opacity and makes ground-based observations nearly impossible and very scarce. However, future space telescopes such as the Heterodyne Instrument for the Far-Infrared (HIFI) on the *Herschel Space Observatory* and the Echelon Cross Echelle Spectrograph (EXES) on the *Stratospheric Observatory for Infrared Astronomy* (SOFIA) will open up new spectral windows which are particularly suited to study water in the Universe.

In this chapter, we discuss the expected characteristics of line emission produced by H_2O at temperatures $T \sim 100 - 1000$ K, present in X-ray irradiated protoplanetary disks and the possible observables for these telescopes. In this study, we will focus on identifying diagnostic H_2O lines that will help to locate the snow-line in disks around T Tauri stars.

6.2 Disk model

The density structure is based on the generic T Tauri disk model of D'Alessio et al. (1999), defined by $M_\star = 0.5\,M_\odot$, $R = 2\,R_\odot$, $T_\star = 4000$ K, $M = 10^{-8}\,M_\odot\,yr^{-1}$. The chemical and thermal structure of a protoplanetary disk is calculated using the code as presented by Glassgold et al. (2004) with minor corrections and updates. Important processes in determining the thermal balance included in the model are X-ray heating, gas-grain heating and cooling, accretion heating, wind-disk heating and line cooling (Lyα, recombination lines, OI fine-structure and forbidden lines, and CO rotational and ro-vibrational lines). The chemical network considers about 125 reactions and 25 species. For the interested reader we refer to Glassgold et al. (2004) for a detailed description of all the physical processes involved. An X-ray luminosity of $L_X = 2 \times 10^{30}$ erg s^{-1} and a thermal spectrum $kT_X = 1$ keV is adopted, characteristic for T Tauri stars (Feigelson et al. 2007).

The X-ray luminosity and spectrum of young stars change with time, and vary from source to source. The Chandra Orion Ultradeep Project (COUP) study of the Orion Nebula Cluster (Getman et al. 2005) found that the X-ray luminosity function spans five orders of magnitude from log $L_X = 27 - 32$ for the entire Orion Nebula Cluster. This is consistent with the findings of Wolk et al. 2005, for a subset of 28 solar-mass stars in the Orion Nebular Cluster with masses in the range $M_\star = 0.9 - 1.2\,M_\odot$, which have a median luminosity of log $L_X = 30.25$ erg s^{-1}. Similar results have been found in the XMM-Newton study of the Taurus-Aurigae cluster (Guedel

et al. 2007; Telleschi et al. 2007), where the X-ray luminosity ranges over three orders of magnitude, $\log L_X = 28-31$.

A number of simplifications are adopted into the model. First, in order to account for the attenuation by X-rays, we calculate the absorption by the amount of gas in the disk between the star and the point of interest. However, scattering of X-ray photons is not considered, which would increase the ionization rate at column densities $N_H \sim 10^{23}-10^{25}$ cm^{-2}, but we do take into account ionization due to ^{26}Al radioactive decay. Second, the thermal balance is calculated at about 45 radial points through a 1D escape probability method, where the photons are allowed to escape in the vertical directions. Third, we do not consider far-ultraviolet (FUV) photons in our model, contrary to the models by Jonkheid et al. (2004, 2007) and Kamp & Dullemond (2004). Unlike X-ray fluxes, FUV fluxes are hard to observe. As a result, FUV fluxes toward star-forming regions are scarce and badly quantified. For normal dust opacities, the FUV opacity is much higher then the X-ray opacity, hence the heating and photodissociation effects of the photons are limited to a thin photon dominated region (PDR) layer near the surface of the disk. Inclusion of FUV photons would solely increase the temperature in the very top layers of the disk especially when PAHs are present, and would be able to dissociate, e.g., H_2O, especially when ambient opacities are low. In contrast, X-rays can penetrate much deeper into the disk and hence are more important than UV photons for the global thermal and molecular characterisation of the disk. Which of these heating agents is more important will depend on the characteristics of the disk and the wavelength under consideration. We will a posteriori check how are conclusions are affected by the neglect of UV processes. Fourth, we assume a flaring disk geometry, which varies continuously from 0.028 to >500 AU. However, the present calculations do not take into account structures such as holes, gaps, and rims, although structural and physical modifications may occur at small and large radii. For example, spectral energy distributions measured with the *Spitzer* IRS indicate the occurrence of inner holes and rims at distances on the order of several AU (Dullemond et al. 2007).

6.2.1 Disk structure

Gas temperatures versus perpendicular column densities are plotted in the left upper panel of Fig. 6.1. For radii $R < 25$ AU, we find that gas temperatures in the upper layer range from $3500-5000$ K. However, the precise gas thermal structure is very sensitive to the computational details (Röllig et al. 2007). Deeper in the disk, the X-rays are attenuated and the density increases toward the mid-plane. This results in a sharp drop in temperature. Note that the gas temperature couples to the dust temperature for column densities $N_H \sim 10^{22}$ cm^{-2}. In the right panel of Fig. 6.1, the fractional water abundances versus perpendicular column densities are

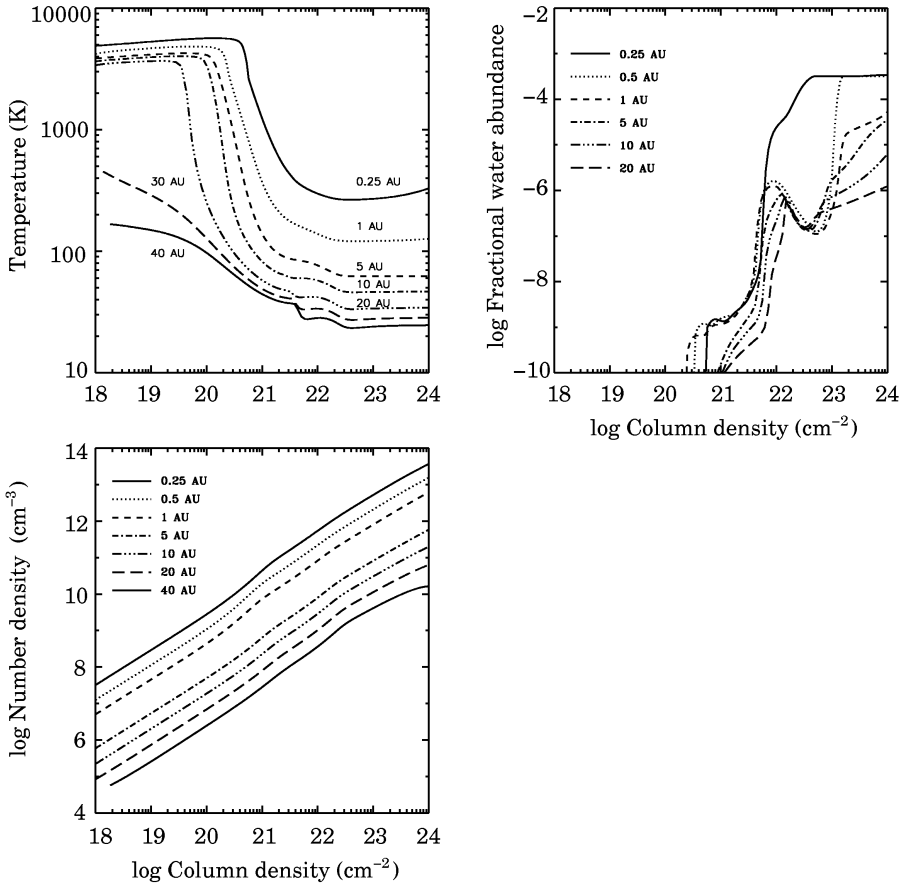

Figure 6.1: Temperature (*Left upper panel*), fractional water abudances (*right panel*) and density structure (*bottom panel*) vs. perpendicular column density for different radii from the central star.

shown. Water abundances are insignificant, i.e., $X(H_2O) < 10^{-10}$, at temperatures $T_g = 3000 - 5000$ K. In the transition zone from atomic to molecular hydrogen, i.e., around $N_H \sim 10^{22}$ cm^{-2}, a peak in the water abundance of $X(H_2O) \sim 10^{-6}$ is found. At even larger column densities ($N_H > 10^{23}$ cm^{-3}), the water abundance increases to values higher than 10^{-5}. Even higher abundances ar found for regions at radii $R \lesssim 0.5$ AU where the gas is warm enough to drive large parts of the oxygen into water, and directly after the H/H$_2$ transition, where water abundances as large as 10^{-4} are found. The bottom panel of Fig. 6.1 plots the adopted density structure. The density spans a large range from 10^4 cm^{-3} to 10^{14} cm^{-3}. The lowest densities are

present in the surface layers, whereas the density increases towards the midplane of the circumstellar disk.

6.3 Radiative transfer

The H_2O line list of the HITRAN database (Rothman et al. 2005) is used to model the rich water spectrum in a protoplanetary disk. In order to make the list manageable for spectral line modeling, we restrict ourselves to those lines with strengths greater than 1% of the strongest line in the region at a temperature of 3000 K. This leaves about 2700 rotational and ro-vibrational transitions, of which $\sim 60\%$ are ortho-transitions.

The pure rotational lines, involving the first 45 o- and p-H_2O levels, are calculated taking into account radiative and collisional (de-)excitation rates using the Leiden Atomic and Molecular Database (LAMDA, Schöier et al. 2005). Higher excitation lines are considered as well, and are to first order assumed to be in thermal equilibrium (LTE). This assumption is appropriate since due to the large densities (up to 10^{14} cm^{-3} in the midplane) the critical density of the transitions is on the order of, or less than the density of the disk. In the top layer, the densities are much lower than the critical densities of most transitions. Hence, the level populations are not in LTE there. However, the water abundance level at these positions in the disk is very low, and therefore will not influence the integrated intensities.

In addition to collisionally (de-)excited rotational and ro-vibrational transitions, we calculate the excitation of fluorescent lines between $5.5-6.5\,\mu$m. We select transitions with an upper level in the first fundamental vibrational mode (with energies up to $\lesssim 2300$ K) and all the levels in the ground-state vibrational mode up to $J=7$. In this way, 53 ortho- and 43 para-H_2O fluorescent transitions are selected. The effect on the resulting fluxes of the fluorescent transitions described throughout this chapter, by taking into account levels up to $J=9$ or higher, is around a factor of 3 or lower. Fluorescent excitation rates are calculated as

$$\sigma_{lu} = \frac{\Omega_\star}{4\pi} n_l \frac{g_u}{g_l} A_{ul} [\exp(hc\nu_{ul}/kT_\star) - 1]^{-1}, \tag{6.1}$$

with g_u, g_l the statistical weights of the upper and lower level, n_l the relative population of the lower level, A_{ul} the Einstein-A coefficient, and $\Omega_\star$ the solid angle of the exciting blackbody. As a consequence, fluorescent excitation rates vary with distance to the star as $\Omega_\star$ is a function of distance. Fluorescent excitation rates of the transitions under consideration are small with respect to the rotational and vibrational Einstein-A coefficients. As a result, the molecules will have enough time to cascade down to the lowest rotational levels between subsequent fluorescence cycles. Therefore, the level populations for fluorescent lines are solely determined by

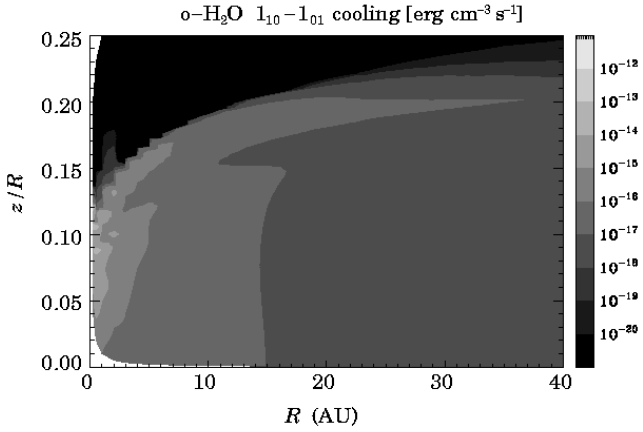

Figure 6.2: Distribution throughout the disk for the ortho-H_2O 1_{10}-1_{01} cooling.

radiative processes, and no collisional rate input is needed.

6.4 Results

6.4.1 Rotational transitions

The pure rotational lines of water considered here have wavelengths between 75 and 1600 μm. These lines are therefore potentially observable by HIFI and the *Photodetector Array Camera and Spectrometer* (PACS) on Herschel. At 34 radii between 0.15 and 100 AU, the emergent intensity as a function of distance z, relative to the disk mid-plane, is calculated.

The flux of a transition $u \rightarrow l$ from a disk annulus between R and R+dR is given by:

$$\mathrm{d}F_{ul} = \frac{1}{4\pi d^2} 2\pi R \mathrm{d}R \int_{z=0}^{z=\infty} \mathrm{d}z' I_{ul}(z'), \tag{6.2}$$

which we use to calculate the fluxes of a face-on disk. The fluxes are calculated for a source located at $d = 140$ pc, the distance to the Taurus star-formation region. The results are listed in Table 6.1. In Fig. 6.2, the distribution of the o-H_2O 1_{10}-1_{01} line is plotted. The highest emissivities are seen at the smallest radii, since both temperatures and densities are the highest there. Some of the lines would in principle be observable within a couple of hours when water would not freeze-out, given a sensitivity of 1.3 – 34×10^{-15} erg cm^{-2} s^{-1} (622 –156 μm) for a 5σ detection within one hour (see *http://herschel.esac.esa.int/*). It is clear from observations of Giant Molecular Clouds by SWAS and ODIN (Snell et al. 2000), however, that this will

Table 6.1: H_2O integrated line fluxes for pure rotational lines in case $L_X = 2 \times 10^{30}$ erg s^{-1}, and a distance to the source of 140 pc. There is one column whithout freeze-out, and three columns with freeze-out at 110 K, and assumed gas-phase H_2O abundances of 10^{-8}, 10^{-10} and 10^{-15} in the freeze-out zone.

Transition	Wavelength	Flux [erg cm^{-2} s^{-1}]			
		no freeze-out	with freeze-out		
	[μm]		10(−8)	10(−10)	10(−15)
o-H_2O 1_{10}-1_{01}	538.3	4.8(−16)	3.9(−16)	1.3(−16)	7.9(−19)
o-H_2O 2_{12}-1_{01}	179.5	2.7(−15)	2.0(−15)	5.7(−16)	1.7(−17)
o-H_2O 2_{21}-1_{10}	108.0	2.9(−15)	1.7(−15)	3.0(−16)	6.5(−17)
o-H_2O 2_{21}-2_{12}	180.5	2.1(−15)	7.9(−16)	5.7(−17)	1.7(−17)
o-H_2O 3_{03}-2_{12}	174.6	2.0(−15)	9.0(−16)	9.0(−17)	1.8(−17)
o-H_2O 3_{12}-2_{21}	259.9	5.7(−16)	8.5(−17)	7.1(−18)	5.6(−18)
o-H_2O 3_{12}-3_{03}	273.2	8.7(−16)	2.2(−16)	1.4(−17)	5.4(−18)
o-H_2O 3_{21}-2_{12}	75.3	3.0(−15)	1.0(−15)	2.0(−16)	1.6(−16)
o-H_2O 3_{21}-3_{12}	257.7	6.6(−16)	1.3(−16)	1.0(−17)	6.4(−18)
o-H_2O 4_{14}-3_{03}	113.5	2.2(−15)	6.4(−16)	8.1(−17)	5.8(−17)
o-H_2O 3_{30}-3_{21}	136.5	7.2(−16)	1.0(−16)	3.6(−17)	3.4(−17)
p-H_2O 1_{11}-0_{00}	269.3	1.8(−15)	1.5(−15)	4.5(−16)	5.4(−18)
p-H_2O 2_{02}-1_{11}	303.4	1.3(−15)	7.5(−16)	6.7(−17)	3.7(−18)
p-H_2O 2_{20}-1_{11}	100.9	7.4(−16)	3.4(−16)	2.3(−17)	1.8(−18)
p-H_2O 2_{11}-2_{02}	398.6	2.5(−15)	1.2(−15)	1.7(−16)	7.6(−17)
p-H_2O 2_{20}-2_{11}	243.9	1.2(−15)	3.1(−16)	1.7(−17)	7.0(−18)
p-H_2O 3_{13}-2_{02}	138.5	2.0(−15)	8.1(−16)	7.9(−17)	3.4(−17)
p-H_2O 3_{13}-2_{20}	1645.7	2.8(−18)	1.4(−19)	2.0(−20)	1.9(−20)
p-H_2O 3_{22}-2_{11}	89.9	2.4(−15)	6.2(−16)	1.2(−16)	1.0(−16)
p-H_2O 4_{04}-3_{13}	125.3	1.3(−15)	4.1(−16)	2.1(−16)	2.1(−16)

NOTE: *a(b)* means $a \times 10^b$

lead to an overestimate of the gas-phase water abundance, since part of the water will freeze-out onto dust grains. However, the remaining gas-phase water abundance is very uncertain when the dust temperature drops below the sublimation temperature. This abundance will depend on uncertain and ill-understood processes as photodesorption and turbulent mixing. Nevertheless, Boonman et al. (2003) concluded from the modelling of water toward massive protostars that the gas-phase water abundance in regions where water freezes-out is lower than 10^{-8}. To account for this, we have opted to simply assume an uniform H_2O abundance when the temperature is below the H_2O sublimation temperature, $T = 110$ K. We adopt gas-phase abundances in the freeze-out zones of 10^{-8}, 10^{-10} and 10^{-15}. The flux reduction in the most favourable case, i.e., $X(H_2O) = 10^{-8}$, ranges between 10 to 80 percent. Most lines will still be observable. This is also the case when

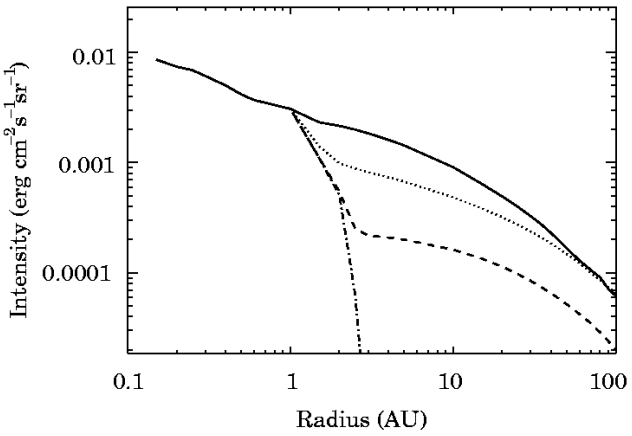

Figure 6.3: Radial profile of the ortho-H_2O 1_{10}-1_{01} line without (*solid line*) and with freeze-out and gas-phase water abundance of 10^{-8} (*dotted*), 10^{-10} (*dashed*) and 10^{-15} (*dash-dotted*).

$X(H_2O) = 10^{-10}$, but becomes impossible for 10^{-15}. In Fig. 6.3, the effect on the radial profile is plotted when freeze-out is included. We find that the bulk of the emission resides within a radius of ~ 3 AU.

6.4.2 Ro-vibrational transitions

EXES on the SOFIA telescope will observe emission between 5 and 28 μm with spectral resolutions of 3, 30 and 100 km s^{-1} – depending on the spectral resolving power, $R = \lambda/\Delta\lambda$, of 10^5, 10^4 and 3000 – and has an angular resolution of 1.5″ at 5 μm. The angular resolution can resolve scales of the order of 200 AU at 140 pc, the distance to Taurus, and is therefore unable to resolve the small radii, $R < 10$ AU, we are considering. Fortunately, the spatial distribution of the emissivity has consequences for the rotational broadening of the lines. Assuming Keplerian rotation for the disk, i.e., $R = GM_\star/v^2$, and a star of $1\,M_\odot$, velocities range from ~ 90 km s^{-1} (0.1 AU) to ~ 17 km s^{-1} (3 AU). In the high resolution mode, EXES is able to resolve the effects on the line shape when water freezes-out at a particular distance from the star, especially at radii $R < 3.0$ AU, where the velocity differences are large.

Note that the dust size distribution in a protoplanetary disk is not necessarily the same as in the interstellar medium. Effects such as photo-evaporation, grain-growth and settling play a major role. As a result, the dust opacity per unit (gas) mass can be much reduced. In the following, we mimic the dust growth by reducing the dust opacity by a factor of 10,

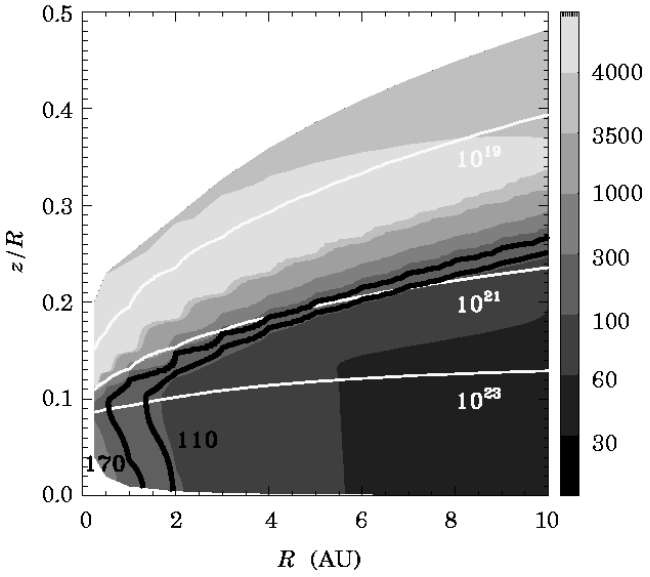

Figure 6.4: Temperature distribution (K) for radii $R = 0 - 10$ AU. The white countours indicate the perpendicular column density at values $N_{\rm H} = 10^{19}$, 10^{21}, and 10^{23} cm^{-2}. The black lines mark the snow line, when it would be situated at 110 K and 170 K, repectively.

100 and 1000. The reduced dust opacities are especially important when fluorescent excitation is considered, as the penetration depth of the photons that are able to fluorescently excite the 6μm lines increases. This leads to an elevated water excitation rate and line fluxes.

Local thermal equilibrium versus fluorescent excitation

Because collisional excitation rates for the ro-vibrational transitions under consideration are not available, and since it would also be numerically challenging to include the full radiative transfer, we first calculate the emission under the assumption that water is fully thermalized (LTE). Moreover, the estimated critical densities, i.e., $n_{\rm cr} = 10^8 - 10^{10}$ cm^{-3}, are close to the densities where most of the water is situated in the disk. Note that when the ambient densities are lower than critical, the obtained emission is an upper limit. The obtained fluxes for all the lines are very small, ranging from $\sim 10^{-18} - 10^{-15}$ erg cm^{-2} s^{-1}, depending on the assumed opacity and the particular line of interest. More importantly, we only find significant emission at very small radii ($R < 0.4$ AU). This would make it impossible to detect

the effects of water freezing-out in the disk, since the snow-line at the mid-plane is expected to be at radii between 1.3 AU – 1.9 AU for this particular protoplanetary disk, when freeze-out temperatures are between 110 K and 170 K. In Fig. 6.4, the temperature distribution is plotted, and the contours indicate the place of the snow-line when it would be at 110 K and 170 K, respectively.

In Table 6.2 – 6.6, we tabulate 21 of the 96 calculated ortho- and para-H_2O line fluxes of the selected transitions as described in Sect. 6.3 for the 'normal' opacities. Table 6.2 lists the results when the level populations are assumed to be in LTE, together with the results when the lines are ascribed to fluorescent excitation, to simplify comparison. Tables 6.3 – 6.6 lists the results for the fluorescent transitions for the different dust opacities and freeze-out temperatures. Some lines are stronger and some are weaker than the LTE calculations. When a line is weaker, there is less flux emitted at small radii, i.e., $R < 0.25$ AU. For all the lines, the emission at large radii, i.e., $R > 1.0$ AU, is enhanced by an order of magnitude compared to LTE, but the total integrated intensities are still weak and unobservable. For lower opacities (see Table 6.4, 6.5, and 6.6), fluorescent excitation is more important than collisional excitation for all lines at all radii, and the unresolved fluxes are a few (when reducing the opacity by 10), up to a 100 times higher (for the lowest opacity). In this way, water is excited further out to radii as far as 5 AU, and still contributes significantly to the total flux, when in the gas-phase. Water beyond a radius of 1 AU is primarily at temperatures below 170 K. As a result, when water freezes-out below a certain temperature – generally assumed to be between 100 K and 170 K – the total flux will be affected. In Tables 6.3 to 6.6, the fluxes are also shown for different freeze-out temperatures (110 K, 145 K and 170 K). The integrated intensities do not change significantly for the 'normal' opacity ($\ll 1\%$), since larger radii are not contributing to the emission, even when there is no freeze-out. This reduction increases from $\sim 10\%$ to $\sim 40\%$ for the highest freeze-out temperatures and for opacities 10 to 1000 times lower than the 'normal' opacity. This is illustrated in Fig. 6.5, for the ortho-H_2O $(010)\,3_{03}$ - $(000)\,3_{12}$ transition. It is seen that the radial profiles change for different freeze-out temperatures, and opacity reductions by factors of 10, 100 and 1000. Cleary, larger radii become increasingly important when the dust opacities are lowered.

Table 6.2: Unresolved fluxes for ro-vibrational transitions, $(v_1v_2v_3)$-$(v'_1v'_2v'_3)$ = (010)-(000), in LTE and by fluorescent excitation (FLUOR) in case the dust opacities are 'normal', and reduced by a factor of 10, 100 and 1000. In this comparison there is no freeze-out included. Fluxes are calculated for $L_X = 2\times10^{30}$ erg s^{-1}, and a distance of 140 pc to the source.

Transition	Wavelength	Flux [erg cm^{-2} s^{-1}]							
	[μm]	'normal dust'		10		100		1000	
		LTE	FLUOR	LTE	FLUOR	LTE	FLUOR	LTE	FLUOR
p-H_2O 1_{11}-2_{20}	6.667	2.2(−16)	9.4(−17)	4.7(−16)	4.9(−16)	4.7(−16)	8.7(−15)	1.1(−15)	2.5(−14)
p-H_2O 4_{04}-4_{13}	6.282	2.2(−16)	1.1(−16)	4.5(−16)	7.2(−16)	4.6(−16)	1.5(−14)	1.1(−15)	4.5(−14)
p-H_2O 3_{31}-4_{22}	6.652	3.5(−17)	2.7(−17)	1.6(−16)	2.7(−16)	2.5(−16)	5.7(−15)	8.2(−16)	2.2(−14)
p-H_2O 2_{11}-2_{02}	6.154	2.1(−16)	1.0(−16)	4.3(−16)	5.7(−16)	4.2(−16)	1.1(−14)	9.9(−16)	3.4(−14)
p-H_2O 2_{20}-2_{11}	6.076	1.6(−16)	6.4(−17)	3.5(−16)	1.8(−16)	3.6(−16)	3.0(−15)	9.0(−16)	1.7(−14)
p-H_2O 4_{04}-3_{13}	5.764	2.0(−16)	1.1(−16)	4.1(−16)	7.3(−16)	4.0(−16)	1.5(−14)	9.5(−16)	4.8(−14)
p-H_2O 6_{06}-5_{15}	5.469	1.9(−16)	1.3(−16)	3.8(−16)	2.0(−15)	3.8(−16)	3.9(−14)	9.4(−16)	1.0(−13)
p-H_2O 4_{22}-3_{13}	5.612	8.5(−17)	5.8(−17)	2.2(−16)	4.3(−16)	2.6(−16)	1.0(−14)	7.0(−16)	4.0(−14)
p-H_2O 4_{40}-3_{31}	5.602	1.1(−16)	7.3(−17)	2.5(−16)	4.6(−16)	2.8(−16)	1.1(−14)	7.3(−16)	4.2(−14)
o-H_2O 4_{14}-5_{05}	6.677	3.0(−16)	2.4(−16)	5.8(−16)	2.1(−15)	5.6(−16)	2.4(−14)	1.3(−15)	5.4(−14)
o-H_2O 5_{05}-5_{14}	6.568	2.7(−16)	2.8(−16)	5.2(−16)	2.5(−15)	5.2(−16)	2.6(−14)	1.3(−15)	6.0(−14)
o-H_2O 3_{03}-3_{12}	6.412	3.0(−16)	2.7(−16)	5.6(−16)	2.4(−15)	5.3(−16)	2.4(−14)	1.2(−15)	5.4(−14)
o-H_2O 1_{01}-1_{10}	6.338	2.9(−16)	2.0(−16)	5.4(−16)	1.4(−15)	5.1(−16)	1.5(−14)	1.1(−15)	3.6(−14)
o-H_2O 4_{23}-3_{30}	6.159	9.2(−17)	1.1(−16)	2.5(−16)	1.2(−15)	3.1(−16)	1.8(−14)	8.8(−16)	4.8(−14)
o-H_2O 2_{12}-1_{01}	6.045	2.5(−16)	1.7(−16)	4.9(−16)	1.4(−15)	4.5(−16)	1.6(−14)	1.0(−15)	4.0(−14)
o-H_2O 4_{32}-5_{05}	5.950	5.5(−18)	1.2(−17)	5.4(−17)	4.5(−16)	1.5(−16)	1.2(−14)	6.2(−16)	4.5(−14)
o-H_2O 2_{21}-1_{10}	5.880	2.2(−16)	1.2(−16)	4.3(−16)	6.6(−16)	4.1(−16)	1.1(−14)	9.3(−16)	3.4(−14)
o-H_2O 3_{21}-2_{12}	5.745	1.8(−16)	1.4(−16)	3.7(−16)	1.1(−15)	3.6(−16)	1.7(−14)	8.5(−16)	4.9(−14)
o-H_2O 5_{32}-5_{05}	5.538	2.0(−17)	4.1(−17)	1.0(−16)	6.9(−16)	1.8(−16)	1.5(−14)	6.1(−16)	5.9(−14)
o-H_2O 5_{41}-5_{14}	5.394	5.6(−18)	2.5(−17)	5.0(−17)	1.0(−15)	1.4(−16)	2.1(−14)	5.4(−16)	7.1(−14)

NOTE: *a(b)* means $a\times10^b$

Table 6.3: Unresolved fluxes for fluorescent ro-vibrational transitions, $(v_1 v_2 v_3)$-$(v'_1 v'_2 v'_3)$ = (010)-(000) in case of 'normal' dust opacities. The freeze-out temperatures are indicated at the top of each column. Fluxes are calculated for $L_X = 2 \times 10^{30}$ erg s^{-1}, and a distance of 140 pc to the source.

Transition	Wavelength	Flux [erg cm^{-2} s^{-1}]			
	[μm]	no	110 K	145 K	170 K
p-H_2O 1_{11}-2_{20}	6.667	9.4(−17)	9.4(−17)	9.4(−17)	9.4(−17)
p-H_2O 4_{04}-4_{13}	6.282	1.1(−16)	1.1(−16)	1.1(−16)	1.1(−16)
p-H_2O 3_{31}-4_{22}	6.652	2.7(−17)	2.7(−17)	2.7(−17)	2.7(−17)
p-H_2O 2_{11}-2_{02}	6.154	1.0(−16)	1.0(−16)	1.0(−16)	1.0(−16)
p-H_2O 2_{20}-2_{11}	6.076	6.4(−17)	6.4(−17)	6.4(−17)	6.4(−17)
p-H_2O 4_{04}-3_{13}	5.764	1.1(−16)	1.1(−16)	1.1(−16)	1.1(−16)
p-H_2O 6_{06}-5_{15}	5.469	1.3(−16)	1.3(−16)	1.3(−16)	1.3(−16)
p-H_2O 4_{22}-3_{13}	5.612	5.8(−17)	5.8(−17)	5.8(−17)	5.8(−17)
p-H_2O 4_{40}-3_{31}	5.602	7.3(−17)	7.3(−17)	7.3(−17)	7.3(−17)
o-H_2O 4_{14}-5_{05}	6.677	2.4(−16)	2.4(−16)	2.4(−16)	2.4(−16)
o-H_2O 5_{05}-5_{14}	6.568	2.8(−16)	2.8(−16)	2.8(−16)	2.8(−16)
o-H_2O 3_{03}-3_{12}	6.412	2.7(−16)	2.7(−16)	2.7(−16)	2.7(−16)
o-H_2O 1_{01}-1_{10}	6.338	2.0(−16)	2.0(−16)	2.0(−16)	2.0(−16)
o-H_2O 4_{23}-3_{30}	6.159	1.1(−16)	1.1(−16)	1.1(−16)	1.1(−16)
o-H_2O 2_{12}-1_{01}	6.045	1.7(−16)	1.7(−16)	1.7(−16)	1.7(−16)
o-H_2O 4_{32}-5_{05}	5.950	1.2(−17)	1.2(−17)	1.2(−17)	1.2(−17)
o-H_2O 2_{21}-1_{10}	5.880	1.2(−16)	1.2(−16)	1.2(−16)	1.2(−16)
o-H_2O 3_{21}-2_{12}	5.745	1.4(−16)	1.4(−16)	1.4(−16)	1.4(−16)
o-H_2O 5_{32}-5_{05}	5.538	4.1(−17)	4.1(−17)	4.1(−17)	4.1(−17)
o-H_2O 4_{41}-3_{30}	5.417	1.5(−16)	1.5(−16)	1.5(−16)	1.5(−16)

NOTE: *a(b)* means $a \times 10^b$

Table 6.4: Unresolved fluxes for fluorescent ro-vibrational transitions, $(v_1v_2v_3)$-$(v'_1v'_2v'_3)$ = (010)-(000) in case the dust opacities are reduced by a factor of 10. The freeze-out temperatures are indicated at the top of each column. Fluxes are calculated for $L_X = 2 \times 10^{30}$ erg s^{-1}, and a distance of 140 pc to the source.

Transition	Wavelength	Flux [erg cm^{-2} s^{-1}]			
	[μm]	no	110 K	145 K	170 K
p-H_2O 1_{11}-2_{20}	6.667	4.9(−16)	4.7(−16)	4.6(−16)	4.5(−16)
p-H_2O 4_{04}-4_{13}	6.282	7.2(−16)	6.9(−16)	6.7(−16)	6.6(−16)
p-H_2O 3_{31}-4_{22}	6.652	2.7(−16)	2.6(−16)	2.6(−16)	2.5(−16)
p-H_2O 2_{11}-2_{02}	6.154	5.7(−16)	5.5(−16)	5.4(−16)	5.3(−16)
p-H_2O 2_{20}-2_{11}	6.076	1.8(−16)	1.8(−16)	1.7(−16)	1.7(−16)
p-H_2O 4_{04}-3_{13}	5.764	7.3(−16)	6.9(−16)	6.8(−16)	6.6(−16)
p-H_2O 6_{06}-5_{15}	5.469	2.0(−15)	1.9(−15)	1.9(−15)	1.8(−15)
p-H_2O 4_{22}-3_{13}	5.612	4.3(−16)	4.1(−16)	4.0(−16)	3.9(−16)
p-H_2O 4_{40}-3_{31}	5.602	4.6(−16)	4.3(−16)	4.2(−16)	4.1(−16)
o-H_2O 4_{14}-5_{05}	6.677	2.1(−15)	2.0(−15)	1.9(−15)	1.9(−15)
o-H_2O 5_{05}-5_{14}	6.568	2.5(−15)	2.3(−15)	2.3(−15)	2.2(−15)
o-H_2O 3_{03}-3_{12}	6.412	2.4(−15)	2.3(−15)	2.2(−15)	2.2(−15)
o-H_2O 1_{01}-1_{10}	6.338	1.4(−15)	1.3(−15)	1.3(−15)	1.3(−15)
o-H_2O 4_{23}-3_{30}	6.159	1.2(−15)	1.1(−15)	1.1(−15)	1.1(−15)
o-H_2O 2_{12}-1_{01}	6.045	1.4(−15)	1.3(−15)	1.3(−15)	1.3(−15)
o-H_2O 4_{32}-5_{05}	5.950	4.5(−16)	4.3(−16)	4.3(−16)	4.2(−16)
o-H_2O 2_{21}-1_{10}	5.880	6.6(−16)	6.2(−16)	6.1(−16)	5.9(−16)
o-H_2O 3_{21}-2_{12}	5.745	1.1(−15)	1.0(−15)	1.0(−15)	9.8(−16)
o-H_2O 5_{32}-5_{05}	5.538	6.9(−16)	6.6(−16)	6.5(−16)	6.3(−16)
o-H_2O 5_{41}-5_{14}	5.394	1.0(−15)	9.9(−16)	9.8(−16)	9.5(−16)

NOTE: *a(b)* means $a \times 10^b$

Table 6.5: Unresolved fluxes for fluorescent ro-vibrational transitions, $(v_1v_2v_3)$-$(v'_1v'_2v'_3)$ = (010)-(000) in case the dust opacities are reduced by a factor of 100. The freeze-out temperatures are indicated at the top of each column. Fluxes are calculated for $L_X = 2 \times 10^{30}$ erg s^{-1}, and a distance of 140 pc to the source.

Transition	Wavelength	Flux [erg cm^{-2} s^{-1}]			
	[μm]	no	110 K	145 K	170 K
p-H_2O 1_{11}-2_{20}	6.667	8.7(−15)	7.3(−15)	6.5(−15)	6.0(−15)
p-H_2O 4_{04}-4_{13}	6.282	1.5(−14)	1.2(−14)	1.1(−14)	1.0(−14)
p-H_2O 3_{31}-4_{22}	6.652	5.7(−15)	5.0(−15)	4.5(−15)	4.1(−15)
p-H_2O 2_{11}-2_{02}	6.154	1.1(−14)	9.6(−15)	8.5(−15)	7.9(−15)
p-H_2O 2_{20}-2_{11}	6.076	3.0(−15)	2.6(−15)	2.4(−15)	2.2(−15)
p-H_2O 4_{04}-3_{13}	5.764	1.5(−14)	1.3(−14)	1.1(−14)	1.0(−14)
p-H_2O 6_{06}-5_{15}	5.469	3.9(−14)	3.2(−14)	2.9(−14)	2.6(−14)
p-H_2O 4_{22}-3_{13}	5.612	1.0(−14)	8.9(−15)	8.0(−15)	7.3(−15)
p-H_2O 4_{40}-3_{31}	5.602	1.1(−14)	9.6(−15)	8.6(−15)	7.9(−15)
o-H_2O 4_{14}-5_{05}	6.677	2.4(−14)	1.9(−14)	1.7(−14)	1.6(−14)
o-H_2O 5_{05}-5_{14}	6.568	2.6(−14)	2.1(−14)	1.9(−14)	1.8(−14)
o-H_2O 3_{03}-3_{12}	6.412	2.4(−14)	2.0(−14)	1.7(−14)	1.6(−14)
o-H_2O 1_{01}-1_{10}	6.338	1.5(−14)	1.3(−14)	1.1(−14)	1.0(−14)
o-H_2O 4_{23}-3_{30}	6.159	1.8(−14)	1.5(−14)	1.4(−14)	1.3(−14)
o-H_2O 2_{12}-1_{01}	6.045	1.6(−14)	1.4(−14)	1.2(−14)	1.1(−14)
o-H_2O 4_{32}-5_{05}	5.950	1.2(−14)	1.1(−14)	9.9(−15)	9.4(−15)
o-H_2O 2_{21}-1_{10}	5.880	1.1(−14)	9.9(−15)	8.9(−15)	8.4(−15)
o-H_2O 3_{21}-2_{12}	5.745	1.7(−14)	1.5(−14)	1.3(−14)	1.3(−14)
o-H_2O 5_{32}-5_{05}	5.538	1.5(−14)	1.5(−14)	1.3(−14)	1.2(−14)
o-H_2O 5_{41}-5_{14}	5.394	2.1(−14)	1.9(−14)	1.7(−14)	1.6(−14)

NOTE: *a(b)* means $a \times 10^b$

Table 6.6: Unresolved fluxes for fluorescent ro-vibrational transitions, $(v_1v_2v_3)$-$(v'_1v'_2v'_3)$ = (010)-(000) in case the dust opacities are reduced by a factor of 1000. The freeze-out temperatures are indicated at the top of each column. Fluxes are calculated for $L_X = 2 \times 10^{30}$ erg s^{-1}, and a distance of 140 pc to the source.

Transition	Wavelength	Flux [erg cm^{-2} s^{-1}]			
	[μm]	no	110 K	145 K	170 K
p-H_2O 1_{11}-2_{20}	6.667	2.5(−14)	1.9(−14)	1.7(−14)	1.6(−14)
p-H_2O 4_{04}-4_{13}	6.282	4.5(−14)	3.4(−14)	3.0(−14)	2.8(−14)
p-H_2O 3_{31}-4_{22}	6.652	2.2(−14)	1.8(−14)	1.6(−14)	1.5(−14)
p-H_2O 2_{11}-2_{02}	6.154	3.4(−14)	2.6(−14)	2.3(−14)	2.2(−14)
p-H_2O 2_{20}-2_{11}	6.076	1.7(−14)	1.4(−14)	1.3(−14)	1.2(−14)
p-H_2O 4_{04}-3_{13}	5.764	4.8(−14)	3.7(−14)	3.3(−14)	3.0(−14)
p-H_2O 6_{06}-5_{15}	5.469	1.0(−13)	7.8(−14)	6.9(−14)	6.5(−14)
p-H_2O 4_{22}-3_{13}	5.612	4.0(−14)	3.1(−14)	2.8(−14)	2.6(−14)
p-H_2O 4_{40}-3_{31}	5.602	4.2(−14)	3.3(−14)	2.9(−14)	2.7(−14)
o-H_2O 4_{14}-5_{05}	6.677	5.4(−14)	4.0(−14)	3.4(−14)	3.2(−14)
o-H_2O 5_{05}-5_{14}	6.568	6.0(−14)	4.4(−14)	3.8(−14)	3.5(−14)
o-H_2O 3_{03}-3_{12}	6.412	5.4(−14)	4.0(−14)	3.4(−14)	3.2(−14)
o-H_2O 1_{01}-1_{10}	6.338	3.6(−14)	2.6(−14)	2.3(−14)	2.1(−14)
o-H_2O 4_{23}-3_{30}	6.159	4.8(−14)	3.6(−14)	3.1(−14)	2.9(−14)
o-H_2O 2_{12}-1_{01}	6.045	4.0(−14)	3.0(−14)	2.6(−14)	2.4(−14)
o-H_2O 4_{32}-5_{05}	5.950	4.5(−14)	3.5(−14)	3.1(−14)	2.9(−14)
o-H_2O 2_{21}-1_{10}	5.880	3.4(−14)	2.6(−14)	2.3(−14)	2.1(−14)
o-H_2O 3_{21}-2_{12}	5.745	4.9(−14)	3.7(−14)	3.2(−14)	3.0(−14)
o-H_2O 5_{32}-5_{05}	5.538	5.9(−14)	4.5(−14)	4.0(−14)	3.7(−14)
o-H_2O 5_{41}-5_{14}	5.394	7.1(−14)	5.4(−14)	4.8(−14)	4.4(−14)

NOTE: *a(b)* means $a \times 10^b$

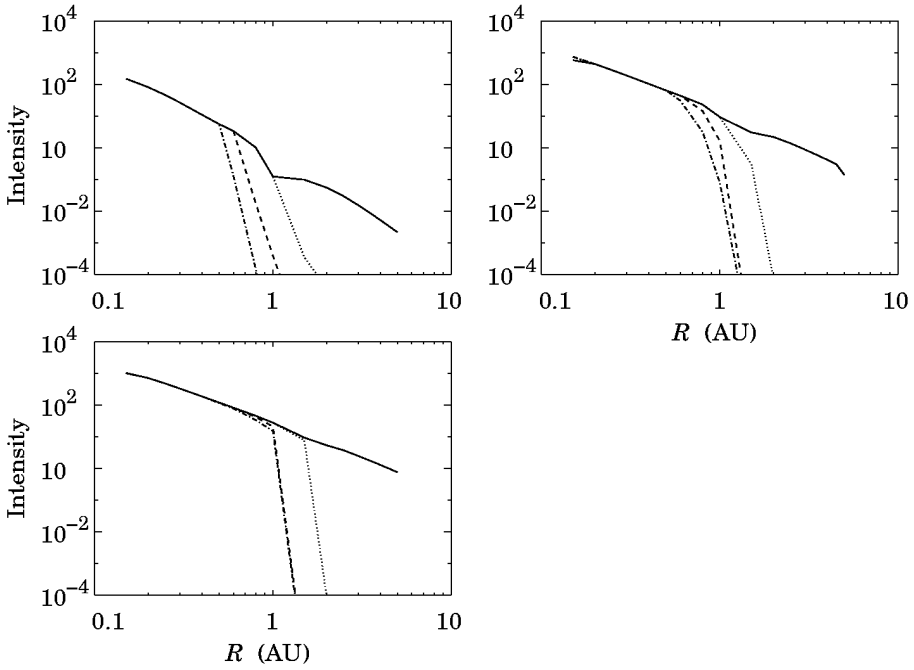

Figure 6.5: Radial intensity profiles for the ortho-H_2O (010) 3_{03} - (000) 3_{12} transition for opacities reduced by factors of 10 (*top left*), 100 (*top right*) and 1000 (*bottom*). The lines indicate no freeze-out (*solid*), freeze-out at 110 (*dotted*), 145 (*dashed*), and 170 K (*dot-dashed*), respectively. The Y-axis is in units of erg s^{-1} cm^{-2} sr^{-1} .

Line ratios

The distribution of the emission throughout a disk differs from one line to another, as a result freeze-out decreases the integrated emission by different amounts depending on the line. In principle, this could provide an estimate of the freeze-out characteristics, e.g., temperature, location of the snow-line, in a particular disk. The reduction of the line emission is between 3 – 10% when the dust opacity is reduced by a factor of 10, and between 25 – 40% when reduced by a factor of 1000, depending on the freeze-out temperature. These reductions are very small and are all of the same order. As a consequence, ratios between these lines do not differ much for different freeze-out temperatures or no freeze-out at all. Therefore, ratios between these lines are not diagnostic in detecting the position of a possible snow-line. However, the transitions are all of energies $E \sim 1500\,\mathrm{cm}^{-1}$.

It would be interesting to look at H_2O lines which have a much higher excitation energy, e.g., around 2.3 μm. These lines will not be affected when freeze-out is included into the models, since it is observed by Carr et al.

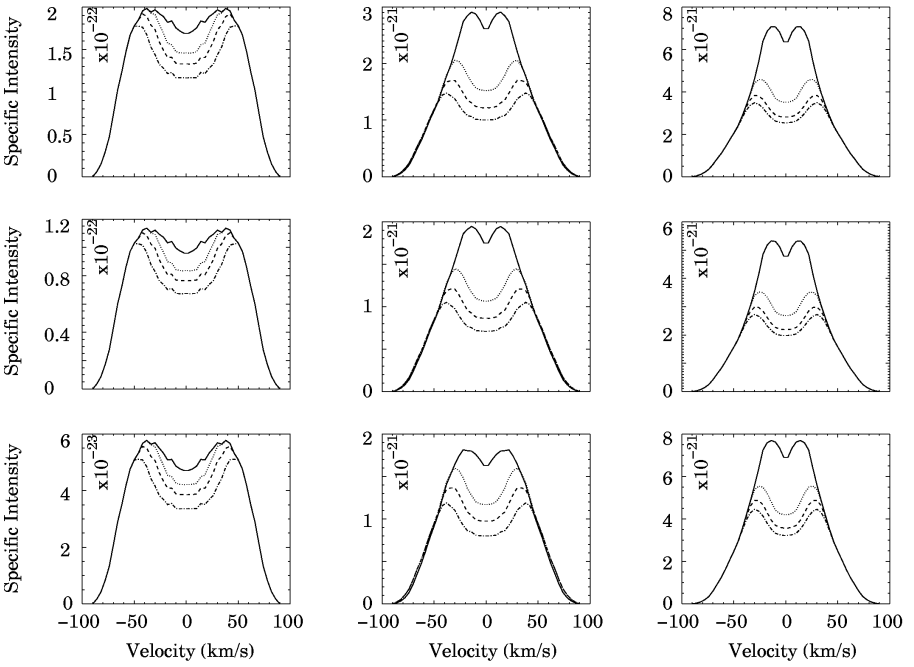

Figure 6.6: Line profile for the ortho-H_2O (010) 3_{03} - (000) 3_{12} (*top*), (010) 2_{12} - (000) 1_{01} (*middle*), and (010) 5_{32} - (000) 5_{05} (*bottom*) transition for opacities reduced by factors of 10 (*left*) 100 (*middle*) and 1000 (*right*) respectively. The different lines represent no-freezout (*solid*), and freeze-out at 110 K (*dotted*), 145 K (*dashed*), and 170 K (*dot-dashed*). The Y-axis is in units of erg s^{-1} cm^{-2} per cm s^{-1}.

(2004) and Thi & Bik (2005) that the emission of these transitions is dominated by regions in the disk close to the star, i.e., $R \sim 0.05 - 0.1$ AU, while the snow-line is much more further out. These observations reveal strong line emission, which would either require large water columns in LTE at high temperatures ($T \sim 1500$ K), or fluorescent excitation. Fluorescent excitation is favoured, since the large column densities needed in LTE are not produced by our model. Of course, other processes such as vertical mixing may also play a role.

6.4.3 Line profiles

Freeze-out does not readily have an effect on ratios between the lines under consideration. However, the emission is reduced in a very specific region in the disk, and this is expected to have an effect on the line shapes. Here we calculate line profiles in a simple way. The disk is assumed to be in Keplerian rotation, although Shu et al. (2007) suggest that deviations may occur

under the influence of magnetic fields. The observed velocity for emission at each point in the disk is then given by:

$$v_{\rm obs}(R,\ \phi,\ i)\ =\ \sqrt{\frac{GM_\star}{R}}\sin(\phi)\sin(i), \tag{6.3}$$

where $(R,\ \phi,\ i)$ represents the place in the midplane of the disk in cylindrical coordinates and i is the inclination angle of the disk. We also assume that the emission escaping the surface of the disk is uniformly emitted in every direction. For simplicity, we consider line profiles for edge-on disks. For these disks, most of the emission will be blocked by the flaring outer parts. However, we will directly look into the center of disks for an inclination $i < 45^\circ$ or smaller. Then, the line profiles will be smaller by a factor $\sin(i)/\sin(90^\circ)$. In Fig. 6.6, line profiles are plotted for the o-H_2O (010) 3_{03} - (000) 3_{12}, (010) 2_{12} - (000) 1_{01}, (010) 5_{32} - (000) 5_{05} transitions for models with reduced dust opacities by a factor of 10, 100 and 1000, with respect to the normal opacities. Models with the 'normal' opacity do not show any change in the line shape, since all the emission of the lines is produced within a radius $R < 1$ AU, and are therefore not plotted. For the models where no water is frozen-out, two peaks are seen, located at velocities between $v = \pm 13$ and $\pm 40\,{\rm km\,s^{-1}}$. When water freezes-out, these two peaks shift towards larger velocities. For models with a reduced dust opacity by a factor of 10, the shift in the peak velocity is small. However, for lower dust opacities, i.e., 100 and 1000 times reduced, the difference is much larger. Even for the lowest freeze-out temperature, i.e., at 110 K, the shift of each peak is more than $10\,{\rm km\,s^{-1}}$, and therefore the velocity difference between the peaks increases by more than $20\,{\rm km\,s^{-1}}$. EXES on board of SOFIA, when observing at a resolution of $3\,{\rm km\,s^{-1}}$, will be able to detect this effect. It will also be possible to say something about the temperature at which the H_2O freezes-out, since the lines shift even more for freeze-out temperatures of 145 and 170 K. Unfortunately, the differences are not very pronounced, especially for the lowest dust opacity. We will get better constraints, however, with a multi-line approach.

6.5 Conclusions

In this chapter, we have constructed models to study the excitation of water in a protoplanetary disk. In this, numerical simulations that produce the thermal structure of X-ray irradiated disks are combined with radiative transfer tools. We have found that (*i*) rotational water lines, observable with HIFI and PACS, will be marginally detectable, when there is no freeze-out in the disk, or when the remaining gas-phase abundances are between 10^{-10} and 10^{-8} in the freeze-out zone. However, the lines will be undetectable for lower remaining gas-phase abundances. (*ii*) Ro-vibrational

lines are unobservable, when dominated by collisional excitation, for the amount of water produced in our X-ray irradiated model. However, lines around 2.3 μm are observed to be bright, which requires large hot water column densities or a different excitation mechanism, e.g., fluorescence. Up to now, we have modeled the fluorescent water lines around 6 μm. We find that 6 μm fluorescent excitation increases both the unresolved flux and the region where water emission is produced, for dust opacities which are 10 to 1000 times smaller than the canonical value for the interstellar medium (ISM). Altered dust size distributions are expected, due to dust settling and photo-evaporation of small grains. (*iii*) The reduction of the line intensities varies from 3% to 40% depending on freeze-out and dust opacity. Line ratios between fluorescent transitions around 6 μm are not useful as a diagnostic tool to determine the location of the snow-line. However, in the future, line ratios between 2.3 μm and 6 μm fluorescent lines should be helpful to investigate the position of the snow-line. (*iv*) Line profiles change when water freezes-out, especially for small dust opacities. We have shown that there is a clear shift in the peak velocities, which is observable within the available velocity resolution of EXES on SOFIA.

References

Andersson, S., Al-Halabi, A., Kroes, G.-J., & van Dishoeck, E. F. 2006, J. Chem. Phys., 124, 4715
Boonman, A. M. S., Doty, S. D., van Dishoeck, E. F., et al. 2003, A&A, 406, 937
Carr, J. S., Tokunaga, A. T., & Najita, J. 2004, ApJ, 603, 213
D'Alessio, P., Calvet, N., Hartmann, L., Lizano, S., & Cantó, J. 1999, ApJ, 527, 893
Dullemond, C. P., Hollenbach, D., Kamp, I., & D'Alessio, P. 2007, Protostars and Planets V, 555
Feigelson, E. D., Broos, P., Gaffney, III, J. A., et al. 2002, ApJ, 574, 258
Garaud, P., & Lin, D. N. C. 2007, ApJ, 654, 606
Getman, K. V., Flaccomio, E., Broos, P. S., et al. 2005, ApJS, 160, 319
Glassgold, A. E., Najita, J., & Igea, J. 2004, ApJ, 615, 972
Güdel, M., Briggs, K. R., Arzner, K., et al. 2007, A&A, 468, 353
Hayashi, C. 1981, Progress of Theoretical Physics Supplement, 70, 35
Jonkheid, B., Faas, F. G. A., van Zadelhoff, G.-J., & van Dishoeck, E. F. 2004, A&A, 428, 511
Jonkheid, B., Dullemond, C. P., Hogerheijde, M. R., & van Dishoeck, E. F. 2007, A&A, 463, 203
Kamp, I., & Dullemond, C. P. 2004, ApJ, 615, 991
Lecar, M., Podolak, M., Sasselov, D., & Chiang, E. 2006, ApJ, 640, 1115
Morbidelli, A., Chambers, J., Lunine, J. I., et al. 2000, Meteoritics and Planetary Science, 35, 1309
Podolak, M., & Zucker, S. 2004, Meteoritics and Planetary Science, 39, 1859
Röllig, M., Abel, N. P., Bensch, F., et al. 2007, A&A, 467, 187
Rothman, L. S., Jacquemart, D., Barbe, A., et al. 2005, Journal of Quantitative Spectroscopy and Radiative Transfer, 96, 139
Sasselov, D. D., & Lecar, M. 2000, ApJ, 528, 995
Schöier, F. L., van der Tak, F. F. S., van Dishoeck, E. F., & Black, J. H. 2005, A&A, 432, 369
Shu, F. H., Galli, D., Lizano, S., Glassgold, A. E., & Diamond, P. H. 2007, ArXiv e-prints, 705
Snell, R. L., Howe, J. E., Ashby, M. L. N., et al. 2000, ApJ, 539, L101

Telleschi, A., Güdel, M., Briggs, K. R., Audard, M., & Palla, F. 2007, A&A, 468, 425
Thi, W.-F., & Bik, A. 2005, A&A, 438, 557
Westley, M. S., Baragiola, R. A., Johnson, R. E., & Baratta, G. A. 1995, Nature, 373, 405
Wolk, S. J., Harnden, Jr., F. R., Flaccomio, E., et al. 2005, ApJS, 160, 423